Comput. Methods Appl. Mech. Engrg. 200 (2011) 917–930

Contents lists available at ScienceDirect

Comput. Methods Appl. Mech. Engrg.

journal homepage: www.elsevier.com/locate/cma

Continuum damage model for orthotropic materials: Application to masonry

Luca Pelà [a,*], Miguel Cervera [b], Pere Roca [b]

[a] DICAM Department, University of Bologna, Viale Risorgimento 2, 40136 Bologna, Italy
[b] International Centre for Numerical Methods in Engineering (CIMNE), Technical University of Catalonia (UPC), Edificio C1, Campus Norte, Jordi Girona 1-3, 08034 Barcelona, Spain

ARTICLE INFO

Article history:
Received 25 June 2009
Received in revised form 25 October 2010
Accepted 15 November 2010
Available online 23 November 2010

Keywords:
Continuum damage mechanics
Orthotropy
Mapping
Transformation tensor
Damage surface
Masonry

ABSTRACT

This paper contributes to the formulation of continuum damage models for orthotropic materials under plane stress conditions. Two stress transformation tensors, related to tensile and compressive stress states, respectively, are used to establish a one-to-one mapping relationship between the orthotropic behaviour and an auxiliary model. This allows the consideration of two individual damage criteria, according to different failure mechanisms, i.e. cracking and crushing. The constitutive model adopted in the mapped space makes use of two scalar variables which monitor the local damage under tension and compression, respectively. The model affords the simulation of orthotropic induced damage, while also accounting for unilateral effects, thanks to a stress tensor split into tensile and compressive contributions. The fundamentals of the method are presented together with the procedure utilized to adjust the model in order to study the mechanical behaviour of masonry material. The validation of the model is carried out by means of comparisons with experimental results on different types of orthotropic masonry at the material level.

1. Introduction

Masonry is a composite material characterized by an overall anisotropic behaviour from the phenomenological point of view [1,2]. This is due to the composite and heterogeneous structure reflecting the particular geometrical arrangement of units and mortar joints. Researchers have provided micro-modelling and macro-modelling techniques for the analysis of masonry [3]. In the former approaches, the discretization is carried out at the level of the components, i.e. units and mortar joints. In the latter approaches, the whole material is regarded as an equivalent homogeneous orthotropic continuum because fully anisotropic description is not readily available.

Early micro-modelling of masonry is due to Page [4], whereas early macro-modelling is due to Samarasinghe et al. [5]. From then on, the micro-modelling approach has experienced larger development in spite of its high computational costs. Macro-modelling still appears as an interesting alternative to produce computationally more efficient models. However, the macro-modelling approach finds some difficulty in the description of the orthotropic behaviour in linear as well as in nonlinear ranges.

Existing approaches for the determination of overall elastic properties of masonry are based on the homogenization theory. Such a methodology consists in identifying an elementary cell, which generates an entire panel by regular repetition. In this way, a field problem can be written on the unit cell in order to achieve average values for the homogenized masonry material, starting from the knowledge of the properties of the constituents and the geometry of the elementary cell. Several procedures have been addressed to the definition of the equivalent elastic moduli for brick masonry, see for instance Refs. [6–10].

There have been few attempts to obtain a general failure criterion for masonry because of the difficulties in developing a representative biaxial test and the large number of tests involved. The problem was discussed firstly in [11,12] with reference to the failure of shear walls. The test data of Page [13,14] were interpolated in [15] by means of three elliptic cones which do not correspond with the observed distinct modes of failure, as the authors mentioned. The elliptic cones have been expressed by a second-order tensor polynomial. On the other hand, a failure criterion was proposed in [16] resorting to four different domains for the case of masonry with perforated bricks.

Some authors proposed a single failure surface for the expression of analytical failure models of masonry. For instance, the Tsai–Wu [17] cubic tensor polynomial already available for composite materials was used in [18], whereas a double pyramid with rectangular base was assumed in [19], for which the slopes of the faces correspond to the internal friction angles of the material. The choice of a single failure criterion for masonry leads to inevitable approximations: the non-acceptable fit of Page's experimental values resulting from the Hoffman [20] criterion was demonstrated in [21]. Furthermore, in the framework of computational plasticity, a

* Corresponding author.
E-mail addresses: luca.pela@unibo.it (L. Pelà), miguel.cervera@upc.edu (M. Cervera), pere.roca.fabregat@upc.edu (P. Roca).

0045-7825/$ - see front matter © 2010 Elsevier B.V. All rights reserved.
doi:10.1016/j.cma.2010.11.010

single surface fit of the experimental values would lead to an extremely complex yield surface with a mixed hardening/softening rule in order to describe properly the inelastic behaviour. Since the aforementioned approach is practically non-feasible, an alternative consists in expanding the conventional formulations for isotropic quasi-brittle materials to describe orthotropic behaviour. Such formulations consider, generally, different inelastic criteria for tension and compression, as in [22] where Rankine and Drucker–Prager [23] criteria were assumed. An extension of such approach is presented in [24], where the material admissible field was bounded by a Hill-type yield criterion for compression and a Rankine-type yield criterion for tension. The choice of two failure surfaces provides better agreement with Page's experimental results.

Concerning masonry nonlinear behaviour, in principle, the damage evolution is anisotropic due to the degradation of the heterogeneous structure. Nevertheless, the existing closed-form macro-models devoted to masonry usually combine the initial orthotropy with orthotropic damage, because of the intrinsic complexities of introducing anisotropic behaviour in the nonlinear range. In the field of Continuum Damage Mechanics (CDM) models, the masonry natural axes (i.e. the bed joints and the head joints directions) were assumed also as damage principal axes in [19]. In each direction, two independent scalar damage parameters are assumed, one for compression and one for tension. Their evolution is described by functions derived from those used for isotropic damage of concrete in terms of material fracture energy in tension or compression. With this energy-based approach tensile and compressive softening can be described within the same context, being the underlying failure mechanisms amenable to continuous crack growth at micro-level. Inelastic behaviour in shear, which in micro-models is related to the mode II fracture energy, cannot be directly included in continuum models and hence it is associated with tension and compression modes in a principal stress space. A similar approach was followed in [24] but in the framework of computational plasticity. In tension, an exponential softening law was adopted for the stress–strain diagrams, with different fracture energies along each material axes. Therefore, the principal directions of damage are fixed and aligned with the initial orthotropy axes. Although the model incorporates two different fracture energies, a single scalar internal parameter is used in the plasticity algorithm in order to measure simultaneously the amount of softening in two material axes. In compression, the authors adopted an isotropic parabolic hardening law, followed by a parabolic/exponential softening law with different compressive fracture energies along the material axes.

The closed-form macro-models are efficient and suitable for complex structural computations. A drawback of such an approach lies in difficulties related to the identification of the needed material parameters, since the necessary experimental procedures could be quite expensive and time consuming. The use of homogenization techniques in estimating macro-scale properties from mortar and brick parameters constitutes an option, e.g. [25–34]. An important class of models addresses the aforementioned difficulty by resorting to multi-level or multi-scale methods [35–39] which transfer the identification problem to the scale of constituents. However, such approaches require considerable computational effort when facing real case studies, even if optimization strategies were proposed to attenuate the drawback [40].

This paper presents a continuum damage model in which the orthotropic behaviour is simulated using the concept of mapped stress tensor, firstly introduced in the framework of plasticity by Betten [41,42] and refined by Oller et al. [43–45] afterwards. According to such approach, a mapping relationship is established between the orthotropic behaviour and an auxiliary model. The problem is solved in a mapped space and the results are transported to the real field, with considerable benefits in terms of simplicity and computation costs.

Several enhancements are introduced into the original Betten's theory in order to deal with masonry material. Firstly, the adoption of two stress transformation tensors [46], related to tensile or compressive stress states, permits the consideration of different behaviours in tension and compression. Two individual damage criteria, related to different failure mechanisms, can be assumed accordingly. Secondly, the constitutive model adopted in the mapped space is based on CDM and makes use of two scalar variables which monitor the local damage under tension and compression, respectively.

The paper is organized as follows: firstly, the formulation of the model is presented together with the description of the constitutive relationships adopted. Then, the general theoretical framework is adjusted to the particular case of the masonry material. Finally, the computational representation of complex failure loci obtained by experiments on orthotropic masonries is provided.

2. Definition of the space transformation tensors

The methodology adopted in this work is based on assuming a real anisotropic space of stresses $\boldsymbol{\sigma}$ and a conjugate space of strains $\boldsymbol{\varepsilon}$, such that each of these spaces has its respective image in a mapped space of stresses $\boldsymbol{\sigma}^*$ and strains $\boldsymbol{\varepsilon}^*$, respectively (see Fig. 1). The relationship between these spaces is defined by

$$\boldsymbol{\sigma}^* = \mathbf{A}^{\boldsymbol{\sigma}} : \boldsymbol{\sigma} \quad \text{or} \quad \sigma^*_{ij} = A^{\sigma}_{ijkl}\sigma_{kl}, \tag{1}$$

$$\boldsymbol{\varepsilon}^* = \mathbf{A}^{\boldsymbol{\varepsilon}} : \boldsymbol{\varepsilon} \quad \text{or} \quad \varepsilon^*_{ij} = A^{\varepsilon}_{ijkl}\varepsilon_{kl}, \tag{2}$$

where $\mathbf{A}^{\boldsymbol{\sigma}} \equiv A^{\sigma}_{ijkl}$ and $\mathbf{A}^{\boldsymbol{\varepsilon}} \equiv A^{\varepsilon}_{ijkl}$ are the transformation tensors, for stresses and strains, respectively, relating the mapped space and the real one. These rank four-tensors embody directly the elastic and strength anisotropy of the material [45].

As discussed before, masonry presents different inelastic behaviour, strength and failure mechanism in tension and compression. For these reasons, two distinct damage criteria must be introduced with a constitutive model able to distinguish tension stress states from compression stress states. An essential feature of the proposed model is that a split into tensile and compressive contributions is introduced. Such a split is carried out on the stress tensor, according to [47–54]:

$$\boldsymbol{\sigma}^+ = \sum_{i=1}^{3} \langle \sigma_i \rangle \mathbf{p}_i \otimes \mathbf{p}_i, \tag{3}$$

$$\boldsymbol{\sigma}^- = \boldsymbol{\sigma} - \boldsymbol{\sigma}^+, \tag{4}$$

where σ_i denotes the ith principal stress value from tensor $\boldsymbol{\sigma}$ and $\mathbf{p}_i$ represents the unit vector associated with its respective principal direction. The ramp function indicated by the Macaulay brackets $\langle\cdot\rangle$ returns the value of the enclosed expression if positive, but sets a zero value if negative. As in Eqs. (3) and (4), in the ensuing lines tensile and compressive entities will be pointed out through the using of indices (+) and (−), respectively.

The split shown by Eqs. (3) and (4) can be expressed in an alternative compact form as follows:

$$\boldsymbol{\sigma}^+ = \mathbf{P} : \boldsymbol{\sigma}, \tag{5}$$

$$\boldsymbol{\sigma}^- = (\mathbf{I} - \mathbf{P}) : \boldsymbol{\sigma}, \tag{6}$$

where $\mathbf{I}$ is the rank-four identity tensor and $\mathbf{P}$ is a projection operator such that

$$\mathbf{P} = \sum_{i=1}^{3} H(\sigma_i)\mathbf{p}_i \otimes \mathbf{p}_i \otimes \mathbf{p}_i \otimes \mathbf{p}_i, \tag{7}$$

where $H(\sigma_i)$ denotes the Heaviside function computed for the ith principal stress σ_i.

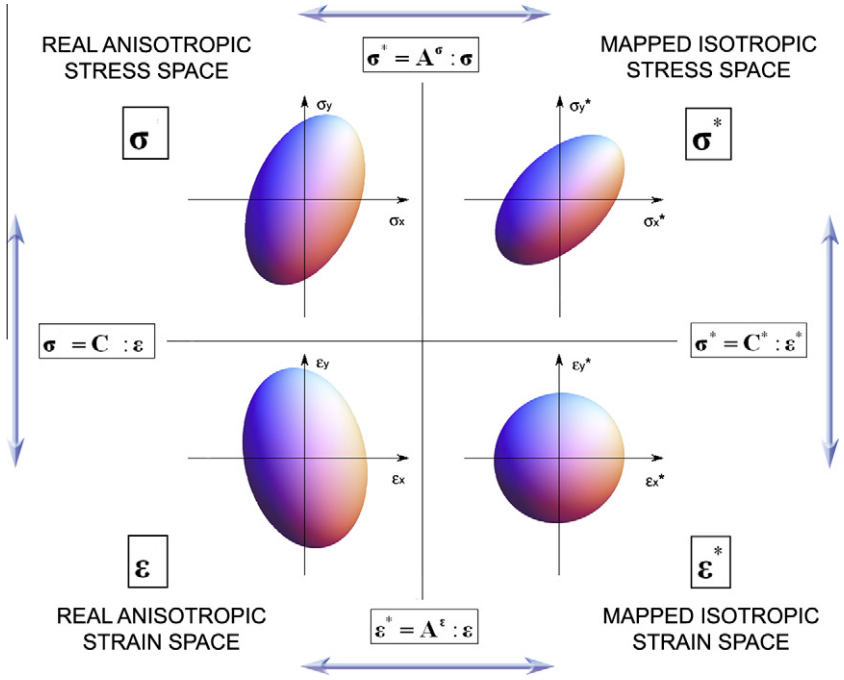

Fig. 1. Relationship between the real anisotropic space and the mapped isotropic space [45].

Differently from Betten's theory, this work proposes distinct transformations of the tensile and compressive stress components from the real to the mapped space [46]:

$$\boldsymbol{\sigma}^{+*} = \mathbf{A}^{\sigma+} : \boldsymbol{\sigma}^{+}, \tag{8}$$

$$\boldsymbol{\sigma}^{-*} = \mathbf{A}^{\sigma-} : \boldsymbol{\sigma}^{-}, \tag{9}$$

where $\mathbf{A}^{\sigma+} \equiv A^{\sigma+}_{ijkl}$ and $\mathbf{A}^{\sigma-} \equiv A^{\sigma-}_{ijkl}$ are the stress transformation tensors, for positive and negative components $\boldsymbol{\sigma}^{+}$ and $\boldsymbol{\sigma}^{-}$, respectively, relating the mapped space and the real one. They are non-singular and positive-definite. The assumption of two distinct stress transformation tensors permits to map the real stresses and solve the problem in an auxiliary workspace, by adopting two different *isotropic* damage criteria for tension and compression.

In this work, plane stress conditions are assumed and the stress space transformation tensors in the (local) material coordinate system (denoted by axes 1 and 2) have the following components:

$$\begin{aligned}
&A^{\sigma\pm\,\prime}_{1111} = f^{\pm *}_{11}/f^{\pm}_{11},\\
&A^{\sigma\pm\,\prime}_{2222} = f^{\pm *}_{22}/f^{\pm}_{22},\\
&A^{\sigma\pm\,\prime}_{1212} = A^{\sigma\pm\,\prime}_{1221} = f^{\pm *}_{12}/(2f^{\pm}_{12}),\\
&A^{\sigma\pm\,\prime}_{2112} = A^{\sigma\pm\,\prime}_{2121} = f^{\pm *}_{12}/(2f^{\pm}_{12}),\\
&A^{\sigma\pm\,\prime}_{1122} = A^{\sigma\pm\,\prime}_{1112} = A^{\sigma\pm\,\prime}_{1121} = 0,\\
&A^{\sigma\pm\,\prime}_{2211} = A^{\sigma\pm\,\prime}_{2212} = A^{\sigma\pm\,\prime}_{2221} = 0,\\
&A^{\sigma\pm\,\prime}_{1211} = A^{\sigma\pm\,\prime}_{1222} = A^{\sigma\pm\,\prime}_{2111} = A^{\sigma\pm\,\prime}_{2122} = 0.
\end{aligned} \tag{10}$$

The assumption of plane stress conditions can be easily modified accounting also for three-dimensional effects due to in-plane loading [55] or even resorting to a complete three-dimensional formulation [45].

Note that from Eq. (10) on, tensors defined in the local coordinate system of the orthotropic material will be marked by apex ($'$).

The parameters $f^{\pm *}_{ii}$, with $i = 1, 2$, are the mapped tensile and compressive strengths along directions 1 and 2. Since we assume two distinct isotropic criteria in the mapped space, it results that $f^{+*}_{11} = f^{+*}_{22} = f^{+*}$ and $f^{-*}_{11} = f^{-*}_{22} = f^{-*}$. The choices of f^{+*} and f^{-*} are arbitrary. The expressions of the mapped shear parameters f^{+*}_{12} and f^{-*}_{12} derive from the particular isotropic criteria adopted for tension and compression.

Assuming a representation of the mapped failure surfaces in terms of stress components σ^*_{11}, σ^*_{22}, τ^*_{12}, the parameters $f^{\pm *}_{ij}$ represent the six intersections of the mapped failure surfaces with the positive and negative branches of the corresponding axes. The parameters $f^{\pm}_{ij}$, on the other hand, represent the intersections with the axes of the failure surfaces defined in the real orthotropic stress space σ_{11}, σ_{22}, τ_{12}. This concept will be detailed in Section 4.1. The orthotropic real strengths $f^{\pm}_{ij}$ can be obtained from adequate experimental tests or homogenization techniques.

The need for two stress transformation tensors to account for different behaviour of the material in tension and compression is evident from (10). Most of all, it always results that $A^{\sigma+\,\prime}_{1212} \neq A^{\sigma-\,\prime}_{1212}$ and the same holds for symmetrical components $A^{\sigma\pm\,\prime}_{1221}$, $A^{\sigma\pm\,\prime}_{2112}$, $A^{\sigma\pm\,\prime}_{2121}$. In fact, it results that $f^{+*}_{12}/f^{+}_{12} \neq f^{-*}_{12}/f^{-}_{12}$ since $f^{+}_{12} \neq f^{-}_{12}$ and $f^{+*}_{12} \neq f^{-*}_{12}$, due to the assumption of distinct damage criteria in tension and compression. Therefore, a single stress transformation tensor would not lead to the correct masonry shear strength. Moreover, such a choice would force the ratio between the tensile and compressive strength to be equal along each axis, whilst in masonry, typically, $f^{-}_{11}/f^{+}_{11} \neq f^{-}_{22}/f^{+}_{22}$.

The stress space transformation tensors in the global coordinate system x_i are readily obtainable from the definitions (10) of the tensor components in the local principal axes x'_i of the orthotropic material. If r_{ij} represents $\cos(x'_i, x_j)$, it results that

$$A^{\sigma\pm}_{ijkl} = r_{pi} r_{qj} r_{rk} r_{sl} A^{\sigma\pm\,\prime}_{pqrs}. \tag{11}$$

It is possible to relate the positive and negative stress transformation tensors to the global stress transformation tensor. In fact, after the definitions (8) and (9), the condition

$$\boldsymbol{\sigma}^* = \boldsymbol{\sigma}^{+*} + \boldsymbol{\sigma}^{-*} \tag{12}$$

must still apply. Therefore, the previous expression yields

$$\begin{aligned}
&\mathbf{A}^{\sigma} : \boldsymbol{\sigma} = \mathbf{A}^{\sigma+} : \boldsymbol{\sigma}^{+} + \mathbf{A}^{\sigma-} : \boldsymbol{\sigma}^{-},\\
&\mathbf{A}^{\sigma} : \boldsymbol{\sigma} = \mathbf{A}^{\sigma+} : \mathbf{P} : \boldsymbol{\sigma} + \mathbf{A}^{\sigma-} : (\mathbf{I} - \mathbf{P}) : \boldsymbol{\sigma}
\end{aligned} \tag{13a, b}$$

and hence [46]

$$\mathbf{A}^{\sigma} = \mathbf{A}^{\sigma+} : \mathbf{P} + \mathbf{A}^{\sigma-} : (\mathbf{I} - \mathbf{P}). \tag{14}$$

The strain space transformation tensor $\mathbf{A}^{\varepsilon}$ can be derived from (1) and the constitutive equation:

$$\mathbf{A}^{\varepsilon} = (\mathbf{C}^{*})^{-1} : \mathbf{A}^{\sigma} : \mathbf{C}, \tag{15}$$

where $\mathbf{C}$ and $\mathbf{C}^{*}$ are the orthotropic and isotropic constitutive tensors defined in the real and mapped space, respectively.

Eq. (15) allows us to derive the relationship between the constitutive tensors in the real and mapped spaces:

$$\mathbf{C} = (\mathbf{A}^{\sigma})^{-1} : \mathbf{C}^{*} : \mathbf{A}^{\varepsilon}. \tag{16}$$

The constitutive tensor $\mathbf{C}$ is expressed in the global reference system. This means that prior to the derivation of the space transformation tensors, the following transformation is required:

$$C_{ijkl} = r_{pi} r_{qj} r_{rk} r_{sl} C'_{pqrs}. \tag{17}$$

3. Underlying damage model

In this section, the description of the CDM model adopted in the mapped space is provided. The present work makes use of the Tension–Compression Damage Model which has been extensively used [47–54]. This model is characterized by two internal scalar variables, which monitor the local damage under tension and compression, respectively. The overall nonlinear behaviour is reproduced including unilateral effects, strain-hardening/softening response, stiffness degradation and regradation under multiple stress reversal.

We recall that in the ensuing lines, apex $(*)$ is assigned to variables related to the mapped space. It is worth noticing that the auxiliary properties, i.e. $f_{ij}^{\pm *}$ and elastic constants in tensor $\mathbf{C}^{*}$, can be selected arbitrarily, since they disappear at the end of the mapping procedure to the auxiliary space and back to the real one.

3.1. Constitutive equations

The Tension–Compression Damage Model adopted in the mapped space is based on a split of the effective stress tensor [56]

$$\bar{\boldsymbol{\sigma}}^{*} = \mathbf{C}^{*} : \boldsymbol{\varepsilon}^{*} \tag{18}$$

into tensile and compressive components, $\bar{\boldsymbol{\sigma}}^{+*}$ and $\bar{\boldsymbol{\sigma}}^{-*}$, in order to account for different behaviours of masonry in tension and compression. According to (3) and (4) it results that:

$$\bar{\boldsymbol{\sigma}}^{+*} = \sum_{j=1}^{3} \left\langle \bar{\sigma}_j^{*} \right\rangle \mathbf{p}_j^{*} \otimes \mathbf{p}_j^{*}, \tag{19}$$

$$\bar{\boldsymbol{\sigma}}^{-*} = \bar{\boldsymbol{\sigma}}^{*} - \bar{\boldsymbol{\sigma}}^{+*}, \tag{20}$$

where $\bar{\sigma}_j^{*}$ denotes the jth principal stress value from tensor $\bar{\boldsymbol{\sigma}}^{*}$ and $\mathbf{p}_j^{*}$ represents the unit vector associated with its respective principal direction.

The split shown by Eqs. (19) and (20) can also be expressed, in compliance with (5) and (6), in the forms

$$\bar{\boldsymbol{\sigma}}^{+*} = \mathbf{P}^{*} : \bar{\boldsymbol{\sigma}}^{*}, \tag{21}$$

$$\bar{\boldsymbol{\sigma}}^{-*} = (\mathbf{I} - \mathbf{P}^{*}) : \bar{\boldsymbol{\sigma}}^{*}, \tag{22}$$

where $\mathbf{P}^{*}$ is a projection operator such that

$$\mathbf{P}^{*} = \sum_{j=1}^{3} H\left(\bar{\sigma}_j^{*}\right) \mathbf{p}_j^{*} \otimes \mathbf{p}_j^{*} \otimes \mathbf{p}_j^{*} \otimes \mathbf{p}_j^{*}. \tag{23}$$

The constitutive equation for the damage model is defined as

$$\boldsymbol{\sigma}^{*} = (1 - d^{+}) \bar{\boldsymbol{\sigma}}^{+*} + (1 - d^{-}) \bar{\boldsymbol{\sigma}}^{-*}, \tag{24}$$

where we have introduced two internal variables, d^{+} and d^{-}, the damage indexes, each related with the sign of the stress and thus with tension and compression. The internal damage variables are equal to zero when the material is undamaged and equal to one when it is completely damaged. Their definition and evolution are detailed afterwards.

Owing to the scalar form of the damage variables d^{+}, d^{-} and to the format of the presented constitutive law, Eq. (24) points out that a split of tensor $\boldsymbol{\sigma}^{*}$ into tensile and compressive tensors $\boldsymbol{\sigma}^{+*}$ and $\boldsymbol{\sigma}^{-*}$ is implicit in the present formulation, that is,

$$\boldsymbol{\sigma}^{+*} = (1 - d^{+}) \bar{\boldsymbol{\sigma}}^{+*}, \tag{25}$$

$$\boldsymbol{\sigma}^{-*} = (1 - d^{-}) \bar{\boldsymbol{\sigma}}^{-*}. \tag{26}$$

This relevant property emphasises that the adopted split of the effective stress tensor leads in fact to a related dual split of the Cauchy stress tensor $\boldsymbol{\sigma}^{*}$.

Although the Tension–Compression Damage Model has been usually termed "isotropic" [47,49,52,54,57], it is possible to demonstrate that the model is definitely orthotropic. In fact, by recalling (21) and (22), (24) can be rewritten as follows:

$$\begin{aligned} \boldsymbol{\sigma}^{*} &= (1 - d^{+}) \mathbf{P}^{*} : \bar{\boldsymbol{\sigma}}^{*} + (1 - d^{-})(\mathbf{I} - \mathbf{P}^{*}) : \bar{\boldsymbol{\sigma}}^{*}, \\ \boldsymbol{\sigma}^{*} &= \left[(1 - d^{+}) \mathbf{P}^{*} + (1 - d^{-})(\mathbf{I} - \mathbf{P}^{*}) \right] : \bar{\boldsymbol{\sigma}}^{*}, \\ \boldsymbol{\sigma}^{*} &= \left[\mathbf{I} - d^{+} \mathbf{P}^{*} - d^{-} (\mathbf{I} - \mathbf{P}^{*}) \right] : \bar{\boldsymbol{\sigma}}^{*} \end{aligned} \tag{27a,b,c}$$

and therefore the constitutive relationship can assume the form

$$\boldsymbol{\sigma}^{*} = (\mathbf{I} - \mathbf{D}) : \bar{\boldsymbol{\sigma}}^{*}, \tag{28}$$

where

$$\mathbf{D} = d^{+} \mathbf{P}^{*} + d^{-} (\mathbf{I} - \mathbf{P}^{*}) \tag{29}$$

is the fourth-order tensor which characterizes the state of damage. As can be easily seen, such a tensor is not isotropic and entails directional orthotropic damage. The dependence on principal directions of stress, expressed by operator $\mathbf{P}^{*}$, is relevant since we have assumed the microcracks and microvoids to growth in different manners under tensile or compressive stress states. If $\mathbf{P}^{*} = \mathbf{I}$, a tensile isotropic damage model is recovered, while if $\mathbf{P}^{*}$ is a zero tensor, we recover a compressive isotropic damage model.

Eq. (29) has a structure similar to (14), used to define the global stress transformation tensor, thus a crucial relationship is emphasized. In fact, the stress transformation in the form (14) has been hypothesized in order to be consistent with the constitutive law to be adopted in the mapped space.

An important remark concerns the distinctive characteristic of the mapped space adopted in the proposed Two-Parameters Damage Model for Orthotropic Materials. The concept of mapping a real anisotropic space into an auxiliary isotropic one, as proposed by Betten [41,42] and Oller et al. [43–45], is not feasible in the presented new framework. In fact, in this particular case the mapped space cannot be termed "isotropic", since we assume an orthotropic damage constitutive law and also a composite damage criterion. Therefore, the present methodology turns the original concept of "mapping the real space into an *isotropic* auxiliary one" into the innovative and more general one of "mapping the real space into a *favourable* (or *convenient*) auxiliary one" [46].

3.2. Damage surfaces in the mapped space

Individual criteria for tension and compression have to be considered in the mapped space, in order to describe different failure mechanisms for masonry. The first criterion is associated with a localized fracture process, namely cracking of the material, and the second criterion is associated with a more distributed fracture

process, viz. crushing of the material. The two damage criteria Φ^{+*} and Φ^{-*} are defined as follows:

$$\Phi^{+*}(\tau^{+*}, r^{+*}) = \tau^{+*} - r^{+*} \leqslant 0, \tag{30}$$

$$\Phi^{-*}(\tau^{-*}, r^{-*}) = \tau^{-*} - r^{-*} \leqslant 0. \tag{31}$$

As shown, since a clear distinction between tension and compression is assumed by means of the stress split defined in (19) and (20), a tensile equivalent stress τ^{+*} and a compressive equivalent stress τ^{-*} have been postulated [47–54] to identify loading, unloading or reloading situations [58].

Variables r^{+*} and r^{-*} are the internal stress-like variables representing the current damage thresholds in tension and compression. Their values control the size of each (monotonically) expanding isotropic damage surface. Notice that the damage criteria are defined in terms of effective stresses. This strategy preserves the advantages of a strain-driven formulation, since the effective stress tensor is itself a strain-based entity, and circumvents the drawbacks inherent to those formulations based on the final Cauchy stress tensor, which require an iterative procedure inside the constitutive model, see [49].

The Kuhn–Tucker relations and the damage consistency conditions control the evolution of the damage bounding surfaces for loading, unloading and reloading conditions

$$\dot{r}^{\pm*} \geqslant 0, \quad \Phi^{\pm*}(\tau^{\pm*}, r^{\pm*}) \leqslant 0, \quad \dot{r}^{\pm*} \cdot \Phi^{\pm*}(\tau^{\pm*}, r^{\pm*}) = 0, \\ \text{if } \Phi^{\pm*}(\tau^{\pm*}, r^{\pm*}) = 0 \text{ then } \dot{r}^{\pm*} \cdot \dot{\Phi}^{\pm*}(\tau^{\pm*}, r^{\pm*}) = 0 \tag{32a, b}$$

leading, in view of (30) and (31), to the loading conditions

$$\dot{\tau}^{\pm*} = \dot{r}^{\pm*}. \tag{33}$$

Therefore, the current values of the internal variables $r^{\pm*}$ are expressed in terms of the current values of τ^{+*} and τ^{-*}, and more precisely in the following form:

$$r^{\pm*} = \max\left[r_0^{\pm*}, \max(\tau^{\pm*})\right], \tag{34}$$

where $r_0^{\pm*} = r_0^{\pm*}(f^{\pm*})$ are the initial values of the damage thresholds and $f^{\pm*}$ are the peak uniaxial strengths.

In the present work, the isotropic Rankine criterion is assumed in the mapped space for tensile stress states. Therefore, the tensile equivalent stress is defined as

$$\tau^{+*} = \langle \bar{\sigma}_1^* \rangle, \tag{35}$$

where $\bar{\sigma}_1^*$ is the largest principal effective stress. The initial value of the damage threshold is

$$r_0^{+*} = f^{+*} \tag{36}$$

where f^{+*} is the peak uniaxial tensile strength.

For compressive stress states, the isotropic criterion proposed by Faria et al. [48,49] is assumed in the mapped space. In this case, the equivalent stress is defined in the following form:

$$\tau^{-*} = \sqrt{3}\left(K\bar{\sigma}_{oct}^{-*} + \bar{\tau}_{oct}^{-*}\right). \tag{37}$$

In this format, directly inspired on the Drucker–Prager criterion, $\bar{\sigma}_{oct}^{-*}$ and $\bar{\tau}_{oct}^{-*}$ are the octahedral normal stress and the octahedral shear stress obtained from $\bar{\sigma}^{-*}$. Constant K controls the aperture of the inherent Drucker–Prager cone. According to (34) and (37), the initial value of the damage threshold is equal to

$$r_0^{-*} = \frac{\sqrt{3}}{3}\left(K - \sqrt{2}\right) f^{-*}. \tag{38}$$

3.3. Evolution of the damage variables. Inelastic behaviour

In the present model, the damage variables $d^+ = d^+(r^{+*})$ and $d^- = d^-(r^{-*})$ are computed according to the evolution laws proposed in [53,54]. Two distinct monotonically increasing functions are assumed such that $0 \leqslant d^{\pm} \leqslant 1$. In tension the softening law takes the exponential form

$$d^+(r^{+*}) = 1 - \frac{r_0^{+*}}{r^{+*}} \exp\left\{2H_{dis}^{+*}\left(\frac{r_0^{+*} - r^{+*}}{r_0^{+*}}\right)\right\}, \tag{39}$$

where the discrete softening parameter $H_{dis}^{+*} \geqslant 0$ is defined as

$$H_{dis}^{+*} = \frac{l_{dis}}{l_{mat}^{+*} - l_{dis}} \tag{40}$$

The discrete crack characteristic width l_{dis} is related to the discrete FE problem and will be detailed in the following. The material characteristic length l_{mat}^{+*} depends only on material mechanical properties and it is defined as

$$l_{mat}^{+*} = \frac{2E^* G_f^{+*}}{(f^{+*})^2}. \tag{41}$$

Since the internal variables and the stresses depend both on strains according to (25) and (34), it is possible to define the $\sigma^{+*}(r^{+*})$ and $d^+(r^{+*})$ relationships for a simple uniaxial tensile problem under monotonically increasing strain, see Fig. 2a. Once the tensile strength f^{+*} is reached, the material begins to soften according to the exponential law (39) and the tensile damage index d^+ increases.

A different law is considered for damage variable d^-, in order to represent the peculiar compressive inelastic behaviour of masonry, see Fig. 2b. The blue line is the piecewise function assumed in this work for $\sigma^{-*}(r^{-*})$ in the case of uniaxial compression. Let us introduce $f_0^{-*} = \eta f^{-*}$, with $0 \leqslant \eta \leqslant 1$, which denotes the stress value at the onset of damage. In such a condition, the size of the bounding

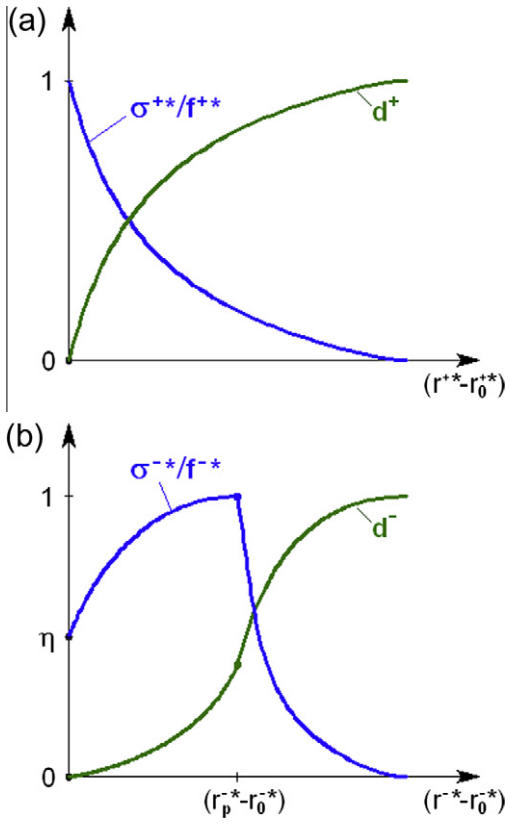

Fig. 2. Evolution laws for damage indexes and total stresses: (a) uniaxial tension and (b) uniaxial compression.

damage surface is established by the value r_0^{-*}. Then, we define the value $r_e^{-*} = r_0^{-*}/\eta$ and the value $r_p^{-*} \geqslant r_e^{-*}$ which corresponds to the size of the bounding damage surface at peak strength f^{-*}. Note that $r_p^{-*} \geqslant r_e^{-*} \geqslant r_0^{-*}$. These terms are necessary to define the hardening/softening response of masonry, which is characterized by a limited ductility in compression. Accordingly, a piecewise function is assumed for $d^-(r^{-*})$, see the green line in Fig. 2b. For parabolic hardening we assume

$$d^-(r^{-*}) = A_d^* \frac{r_e^{-*}}{r^{-*}} \left(\frac{r^{-*} - r_0^{-*}}{r_p^{-*} - r_0^{-*}} \right)^2, \quad r_0^{-*} \leqslant r^{-*} \leqslant r_p^{-*} \tag{42}$$

while for the consequent exponential softening

$$d^-(r^{-*}) = 1 - \frac{r_e^{-*}}{r^{-*}} \exp\left\{ 2H_{dis}^{-*} \left(\frac{r_p^{-*} - r^{-*}}{r_e^{-*}} \right) \right\}, \quad r^{-*} \geqslant r_p^{-*}, \tag{43}$$

where constant A_d^* and the discrete softening parameter $H_{dis}^{-*} \geqslant 0$ are defined as

$$A_d^* = \frac{r_p^{-*} - r_e^{-*}}{r_e^{-*}}, \tag{44}$$

$$H_{dis}^{-*} = \frac{l_{dis}}{l_{mat}^{-*} - \frac{r_p^{-*}}{r_e^{-*}} l_{dis} - 2\overline{A}_d^* l_{dis}} \tag{45}$$

and

$$\overline{A}_d^* = A_d^* \left[\left(r_p^{-*} \right)^3 - 3r_p^{-*} + 2 \right] \Big/ \left[6r_e^{-*} \left(r_p^{-*} - 1 \right)^2 \right], \tag{46}$$

$$l_{mat}^{-*} = \frac{2E^* G_f^{-*}}{\left(f^{-*} \right)^2}. \tag{47}$$

In Eqs. (40) and (45) l_{dis} is the discrete crack characteristic width, i.e. the computational width of the fracture zone in the discrete FE problem, which depends on the finite element size [59]. It has been introduced to regularize the softening modulus, in order to ensure mesh-size objective results, according to [60]. Therefore, the specific dissipated energies D^{+*} and D^{-*} are scaled for each element so that the following equations apply:

$$D^{+*} l_{dis} = G_f^{+*}, \quad D^{-*} l_{dis} = G_f^{-*}. \tag{48a, b}$$

Finally, it is worth mentioning that the analytical derivation of the damaging tangent constitutive tensor for this model is not straightforward. A practical option for such derivation is the numerical differentiation procedure outlined in Refs. [61,62].

4. Damage in the real orthotropic space

4.1. Damage surfaces in the real orthotropic space

In Section 3.2 we have presented the two isotropic damage criteria to be assumed in the mapped space. The expressions (35) and (37) represent the equations of two three-dimensional surfaces defined in the coordinates system denoted by axes σ_x^*, σ_y^*, τ_{xy}^*.

Transformations of stresses (8) and (9) allow us to scale in distinct manners the two isotropic failure surfaces assumed in the mapped space. By means of such a mapping operation, shown in Fig. 3, the desired real orthotropic criteria are reproduced in the coordinate system denoted by axes σ_x, σ_y, τ_{xy}. The corresponding orthotropic composite failure surface is reported in Fig. 4.

Due to the choices of the Rankine and Faria isotropic criteria in the mapped space, the stress transformation tensors components, which have been defined for the general case in (10), are defined as follows:

$$\begin{aligned}
&A_{1111}^{\sigma+\prime} = f^{+*}/f_{11}^+, \\
&A_{2222}^{\sigma+\prime} = f^{+*}/f_{22}^+, \\
&A_{1212}^{\sigma+\prime} = A_{1221}^{\sigma+\prime} = f^{+*}/(2f_{12}^+), \\
&A_{2112}^{\sigma+\prime} = A_{2121}^{\sigma+\prime} = f^{+*}/(2f_{12}^+), \\
&A_{1122}^{\sigma+\prime} = A_{1112}^{\sigma+\prime} = A_{1121}^{\sigma+\prime} = 0, \\
&A_{2211}^{\sigma+\prime} = A_{2212}^{\sigma+\prime} = A_{2221}^{\sigma+\prime} = 0, \\
&A_{1211}^{\sigma+\prime} = A_{1222}^{\sigma+\prime} = A_{2111}^{\sigma+\prime} = A_{2122}^{\sigma+\prime} = 0,
\end{aligned} \tag{49}$$

$$\begin{aligned}
&A_{1111}^{\sigma-\prime} = f^{-*}/f_{11}^-, \\
&A_{2222}^{\sigma-\prime} = f^{-*}/f_{22}^-, \\
&A_{1212}^{\sigma-\prime} = A_{1221}^{\sigma-\prime} = \left[f^{-*} \left(\sqrt{2} - K \right) \Big/ \sqrt{6} \right] \Big/ (2f_{12}^-), \\
&A_{2112}^{\sigma-\prime} = A_{2121}^{\sigma-\prime} = \left[f^{-*} \left(\sqrt{2} - K \right) \Big/ \sqrt{6} \right] \Big/ (2f_{12}^-), \\
&A_{1122}^{\sigma-\prime} = A_{1112}^{\sigma-\prime} = A_{1121}^{\sigma-\prime} = 0, \\
&A_{2211}^{\sigma-\prime} = A_{2212}^{\sigma-\prime} = A_{2221}^{\sigma-\prime} = 0, \\
&A_{1211}^{\sigma-\prime} = A_{1222}^{\sigma-\prime} = A_{2111}^{\sigma-\prime} = A_{2122}^{\sigma-\prime} = 0.
\end{aligned} \tag{50}$$

The choices of f^{+*} and f^{-*} are arbitrary, as explained in Section 3. It is advisable to assume $f^{+*} = f_{11}^+$ and $f^{-*} = f_{11}^-$, in order to obtain $A_{1111}^{\sigma+\prime} = A_{1111}^{\sigma-\prime} = 1$. Such an assumption leads to scale the isotropic criteria only along the second and third cartesian axes, see Fig. 3. It is evident that the transformation of space is feasible only if we know all the six parameters f_{11}^+, f_{11}^-, f_{22}^+, f_{22}^-, f_{12}^+, f_{12}^- , i.e. the strengths of the real orthotropic material. Such parameters also represent the intersections of the real failure surfaces with the cartesian axes, see Fig. 3. They can be derived from the experimental tests on masonry wallets proposed in [63] or from homogenization procedures, as already stressed in Section 1.

As stated in Section 3.2, constant K controls the aperture of the Faria's surface in the mapped space, see Eq. (37). In the new proposed framework, such parameter can be also considered as a fitting parameter of the real failure surface, being related to the real biaxial compressive strength f_{2D}^- according to

$$K = \sqrt{2} \frac{f_{2D}^- \sqrt{\frac{1}{\left(f_{11}^-\right)^2} + \frac{1}{\left(f_{22}^-\right)^2} - \frac{1}{f_{11}^-} \frac{1}{f_{22}^-}} - 1}{f_{2D}^- \left(\frac{1}{f_{11}^-} + \frac{1}{f_{22}^-} \right) - 1} \tag{51}$$

which for $f_{11}^- = f_{22}^-$ leads correctly to the original isotropic expression of K, reported in [48].

4.2. Orthotropic softening behaviour

The model presented in this work is able to describe independent softening behaviour along orthogonal directions, an option typical in masonry macro-modelling [19,63,64].

If the real material is modelled as isotropically softening, according to Eqs. (40) and (41) and (45)–(47) it must result that

$$\frac{2E^* G_f^{\pm*}}{\left(f^{\pm*} \right)^2} = \frac{2E_1 G_{f,1}^{\pm}}{\left(f_{11}^{\pm} \right)^2} = \frac{2E_2 G_{f,2}^{\pm}}{\left(f_{22}^{\pm} \right)^2} \Rightarrow l_{mat}^{\pm*} = l_{mat,1}^{\pm} = l_{mat,2}^{\pm}. \tag{52}$$

The choice of E^*, $f^{\pm*}$, $G_f^{\pm*}$ is arbitrary and so $l_{mat}^{\pm*}$. As already stressed in Section 4.1, it is advisable to assume the mechanical properties in the mapped space such that $E^* = E_1$, $f^{\pm*} = f_{11}^{\pm}$, $G_f^{\pm*} = G_{f,1}^{\pm}$. In this case, it derives from (52) that

$$G_{f,2}^{\pm} = \frac{\left(f_{22}^{\pm} / f_{11}^{\pm} \right)^2}{E_2 / E_1} G_{f,1}^{\pm}, \tag{53}$$

i.e., a restriction on the fracture energy values in the real space, in order to ensure isotropic softening.

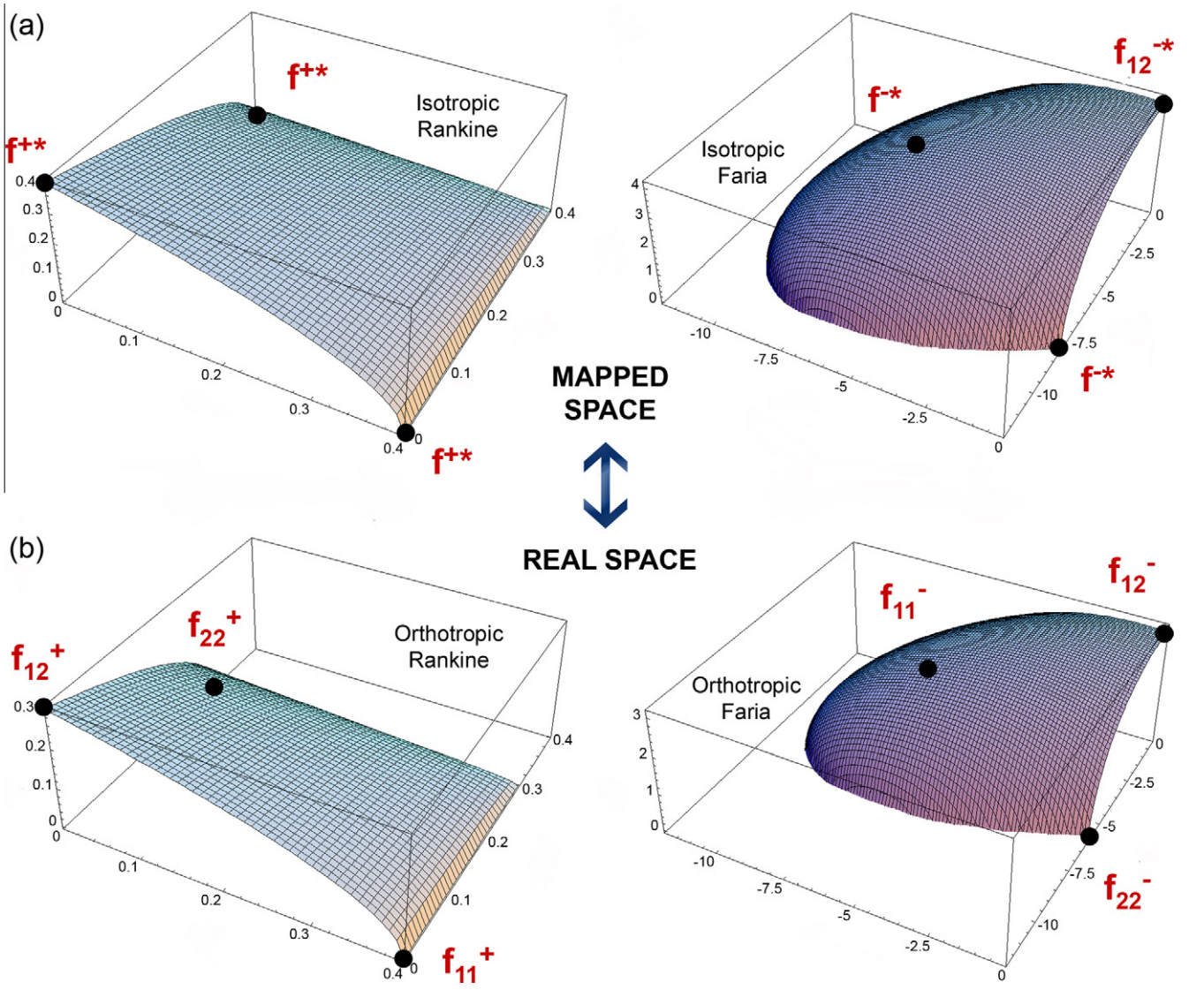

Fig. 3. Adopted failure loci in the mapped space (a) and in the real orthotropic space (b).

The proposed model can also include the description of the orthotropic softening behaviour, which is thought in the sense that the material properties involved in the definition of the expression $d^{\pm} = d^{\pm}(r^{\pm *})$ are directionally dependent. More generally, the rate of the damage indexes

$$\dot{d}^{\pm} = \frac{\partial d^{\pm}}{\partial r^{\pm *}} \dot{r}^{\pm *} \tag{54}$$

is such that $\partial d^{\pm}/\partial r^{\pm *}$ depends on the physical directions. As $r^{\pm *}$ is assumed to behave isotropically and changing such assumption would spoil most of the advantages of the approach, an obvious alternative is to modify $\partial d^{\pm}/\partial r^{\pm *}$ directionally. This procedure "breaks" in some way the basic idea of "isotropy" in the mapped space and it is carried out in a heuristic manner, by using an appropriate directional interpolation between the known values for lengths $l^{\pm}_{mat,1}$ and $l^{\pm}_{mat,2}$. Accordingly, it is possible to represent the orthotropic softening behaviour assuming in the mapped space the following expression for $l^{\pm *}_{mat}$ instead of (52):

$$\frac{1}{\left(l^{\pm *}_{mat}\right)^2} = \frac{1}{\left(l^{\pm}_{mat,1}\right)^2} \cos^2(\alpha - \theta) + \frac{1}{\left(l^{\pm}_{mat,2}\right)^2} \sin^2(\alpha - \theta) \tag{55}$$

in which θ is the angle of orthotropy and α is the angle denoting the direction of the main stress characterized by the maximum absolute value. Both the angles are measured counter clockwise from the global x-axis to the material 1-axis. Expression (55) corresponds exactly to an elliptic interpolation of lengths $l^{\pm}_{mat,1}$ and $l^{\pm}_{mat,2}$ and leads correctly to isotropic softening in case of $l^{\pm}_{mat,1} = l^{\pm}_{mat,2}$. Accordingly, two different softening behaviours can be assumed along the material axes. It suffices to choose the following properties in the mapped space:

$$\begin{aligned} E^* &= E_1, \\ f^{\pm *} &= f^{\pm}_{11}, \\ G^{\pm *}_f &= \frac{(f^{\pm *})^2}{2E^*} l^{\pm *}_{mat}. \end{aligned} \tag{56a,b,c}$$

The presented procedure permits to account for totally different fracture energies along the material axes, providing a full orthotropic softening behaviour. A more fundamental approach would be to define another different mapping between the spaces of the inelastic strains.

The proposed procedure is combined with the regularization presented in Section 3.3 in order to ensure the consistency of the

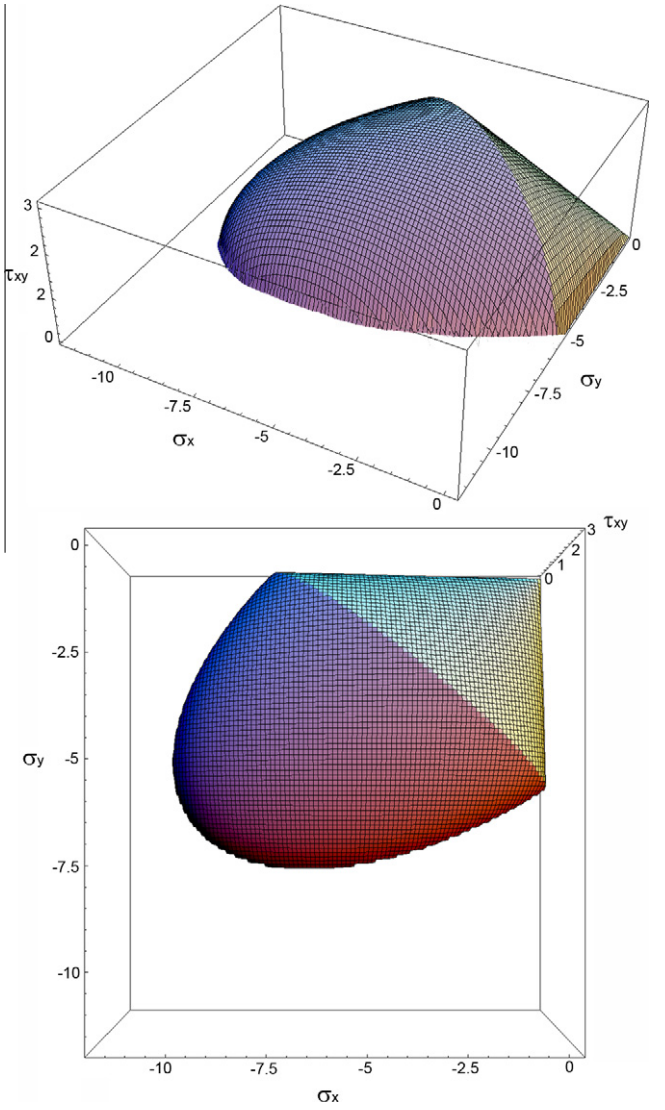

Fig. 4. Orthotropic composite failure surface.

discrete constitutive model with the continuum one, avoiding the mesh size-dependency. The problem of mesh bias-dependency is more general and out of the scope of this paper. In the last three decades, the problem of mesh-bias dependence has been tackled with different approaches (micropolar [65], non-local [66], gradient-enhanced models [67], etc.) which share the standpoint that the original continuum model is not well-posed and it should be modified from the basic, physical, level. This means incorporating the underlying physical collapse mechanism in the formulation. Alternatively, the same problem can be addressed satisfactorily from the numerical point of view in the framework of the definition of the discrete problem associated to crack modelling. The interested reader is referred to [68–73] for details.

As already stressed in Section 1, the degradation in masonry is generally anisotropic and thus it is recognized that the presented approach with orthotropic softening is an approximation. Multi-level or multi-scale methods are able to include the anisotropic evolution of damage depending on the underlying mechanism, although increasing the computational cost. To the authors' knowledge, closed-form macro-models for masonry combining elastic and strength orthotropy with anisotropic degradation are not currently available.

4.3. Inelastic uniaxial behaviour

The uniaxial behaviour of the model is shown in Fig. 5. The considered material properties are listed in Table 1. It can be noticed that the relationship between the fracture energies do not conform with restriction (53). Therefore, the brittleness of the material is not the same along each direction, either in compression or in tension. A tensile exponential softening law is considered, and such a choice is sound for a quasi-brittle material like masonry. Once the fracture energy is exhausted, a no-tension material is recovered.

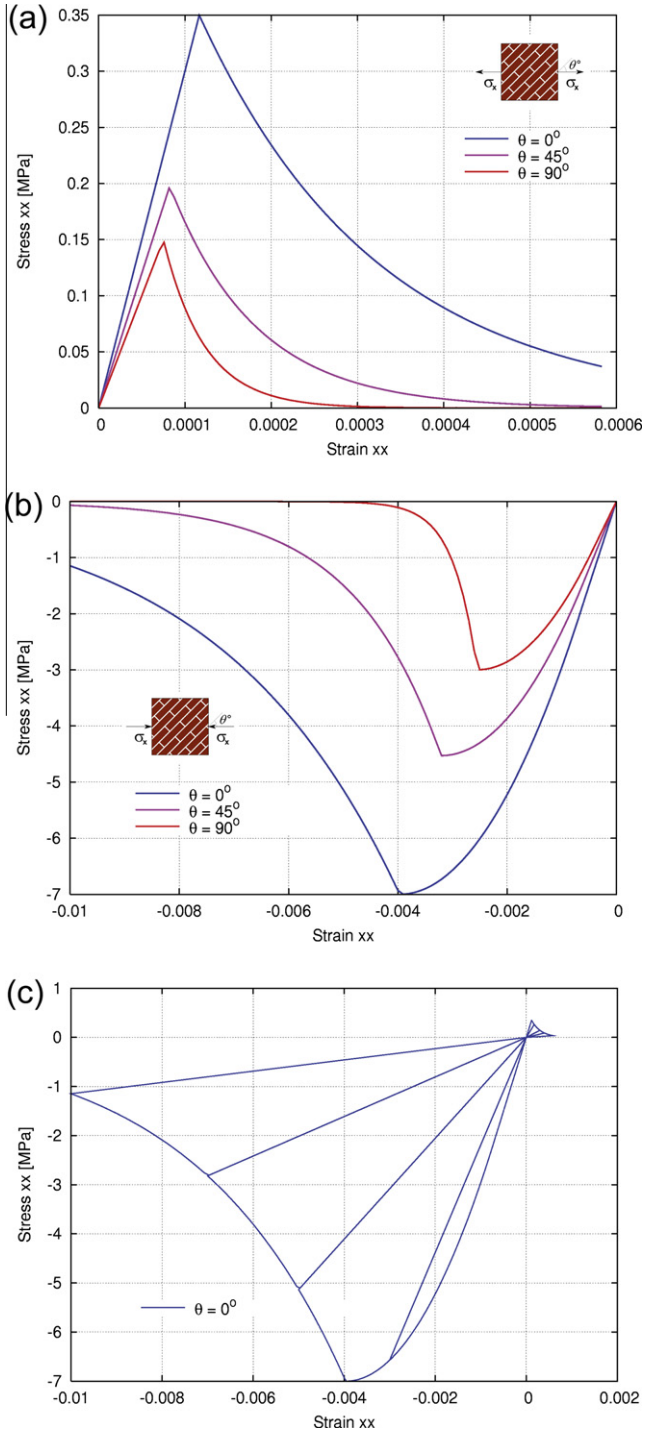

Fig. 5. Uniaxial behaviour of the model: (a) tension, (b) compression and (c) cyclic displacement history.

Table 1
Material properties for uniaxial tension/compression test.

Material properties					
$E_1 = E^*$	3000 MPa	$f_{11}^+ = f^{+*}$	0.35 MPa	$f_1^- = f^{-*}$	7.00 MPa
E_2	2000 MPa	f_{22}^+	0.15 MPa	f_2^-	3.00 MPa
$\nu_{12} = \nu^*$	0.1	f_{12}^+	0.20 MPa	f_{12}^-	3.00 MPa
ν_{21}	0.15	$G_{f,1}^+ = G^{+*}$	100 J/m^2	$G_{f,1}^- = G^{-*}$	40,000 J/m^2
G_{12}	900 MPa	$G_{f,2}^+$	13.8 J/m^2	$G_{f,2}^-$	5510 J/m^2

The material strength in the y-direction degrades at a faster rate than the material strength in the x-direction, see Fig. 5a. The response for the angle of orthotropy $\theta = 45°$ is also reported.

Parabolic hardening followed by exponential softening is considered for the stress–strain diagrams in compression, see Fig. 5b. The peak strength value is assumed to be reached simultaneously on both material axes, i.e. isotropic hardening, followed by orthotropic softening as determined by the different fracture energies. The model allows us to set an ultimate value of the strain, from which the material begins to soften.

The dissimilar behaviour exhibited by masonry under tension or under compression is an essential feature when dealing with cyclic actions. Fig. 5c shows the cyclic response along the material direction 1. As it can be seen, unloading occurs to the origin of the stress–strain diagram, according to a damaged stiffness. A successive reloading follows the same unloading branch, until the damage threshold is reached again. When reversing the sign of the external loading, the constitutive model is able to capture the unilateral behaviour exhibited by masonry and distinguish tension from compression. This is due to the stress split described by Eqs. (19) and (20) and to the definition of two different variables to describe tensile and compressive damage, see Eq. (24). The stiffness recovery upon loading reversal can be represented. For instance, when passing from tension to compression, the model accounts for the crack closure phenomenon in masonry.

5. Validation examples

In this section, the capability of the proposed model to reproduce the strength of different masonry types is demonstrated through a comparison with available experimental data on masonry panels subjected to in-plane loading conditions.

5.1. Simulation of experimental tests conducted by Page

In the early 1980s, Page published the results of a series of tests designed to assess the directional strength characteristics of masonry panels subjected to in-plane monotonic loading. For that purpose, he conducted a series of biaxial compression–compression [13] and biaxial tension–compression [14] tests, which still are the most comprehensive experimental program conducted on the in-plane behaviour of brick masonry. The test specimen consisted of a $360 \times 360 \times 54$ mm^3 panel of running bond brick masonry constructed by adhering the bricks in their designated place to a temporary plate, and then pouring in mortar. A total number of 102 panels were tested. Half-scale bricks were used, where the actual bricks were cut in half in all three dimensions, in order to obtain $115 \times 40 \times 54$ mm^3 elements. In the corners, each individual brick was sawn to the appropriate shape required to fit the designated angle. The specimens were subjected to a biaxial load-controlled test in a load rig. In order to alleviate the restraining effect of the loading caps, a series of brush platens were used to transfer the load to the panel. The tests were conducted for five different orientations, 0°, 22.5°, 45°, 67.5° and 90°, of the principal stress with respect to the direction of the mortar beds. The results from all orientations were then gathered to obtain a comprehensive picture of the directional strength characteristics of brick masonry.

The panels were loaded proportionally in the principal stress directions σ_1 and σ_2 along different orientations θ with respect to the material axes.

The values assumed for orthotropic strengths are $f_{11}^+ = 0.43$ MPa, $f_{22}^+ = 0.32$ MPa and $f_{12}^+ = 0.33$ MPa for tension and $f_{11}^- = 8.74$ MPa, $f_{22}^- = 8.03$ MPa and $f_{12}^- = 2.71$ MPa for compression, according to data given in [14] and parameters calibrated in [63]. The parameter K of Eq. (37) has been considered equal to 0.027, in order to fit accurately the experimental data. The composite damage criterion features a low degree of anisotropy ($f_x^+/f_y^+ = 1.34$ and $f_x^-/f_y^- = 1.09$). For all the tests, the material properties in the 1-axis have been selected for the mapped space.

Fig. 6a–c shows the comparison among the experimental strength values and the failure surfaces corresponding to orientations of the bed joints equal to 0°, 22.5° and 45°, respectively. For the sake of comparison, the failure loci derived by Syrmakezis and Asteris [18] and Lourenço et al. [63] are also depicted. Such models require respectively ten and seven parameters to be defined. The former approach provides a rather adjustable single surface but overestimations are evident along some loading paths. More accurate results are obtained globally with the latter model, thanks to its two surfaces-format, even though some overestimations are encountered. A remarkable agreement is obtained using the proposed model, except for the uniaxial compressive strength parallel to the bed joints which seems to be overpredicted, see Fig. 6a. This is due to a debatable definition of failure in the

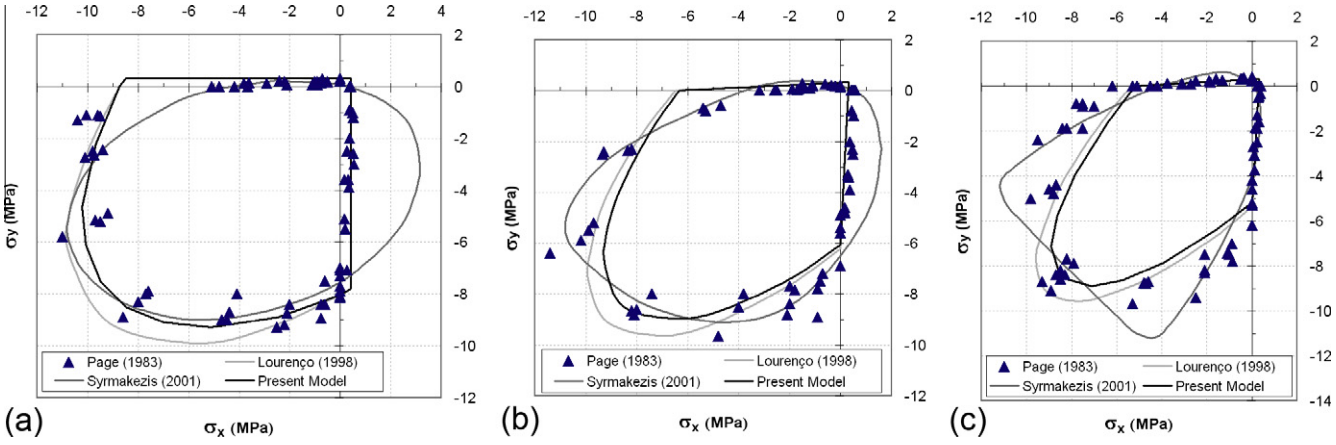

Fig. 6. Comparison among the experimental results from Page [13,14], the proposed model, the models by Lourenço et al. [63] and Syrmakezis and Asteris [18]: (a) $\theta = 0°$; (b) $\theta = 22.5°$ and (c) $\theta = 45°$.

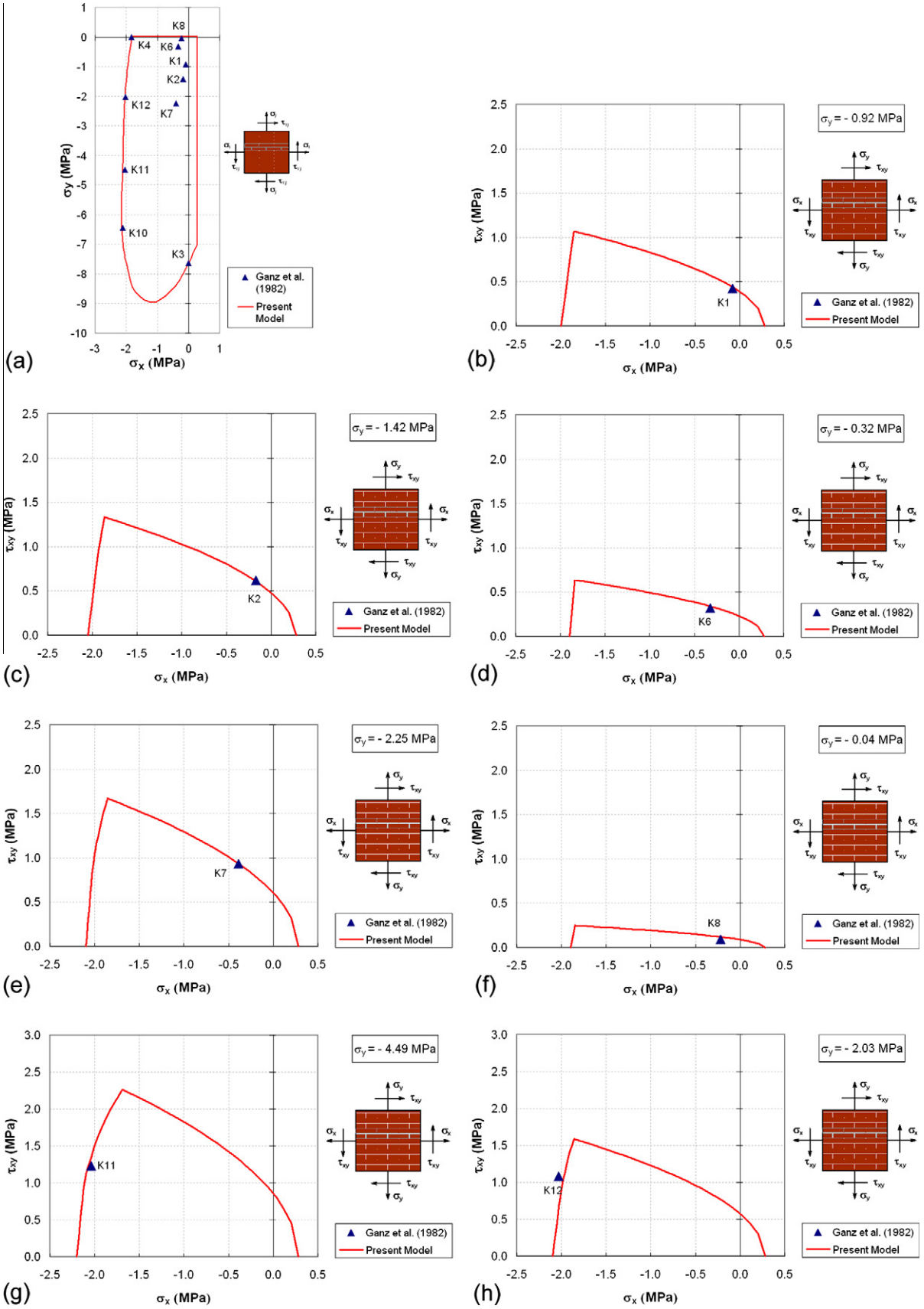

Fig. 7. Comparison between the proposed model and the experimental results from Ganz and Thürlimann [75]: calculated composite failure surface (a) and comparisons with tests K1 (b), K2 (c), K6 (d), K7 (e), K8 (f), K11 (g) and K12 (h).

Table 2
Comparison between the proposed model and the experimental results obtained by Ganz and Thürlimann [75].

Panel	Experimental results			Present model			Ratio
	σ_x (MPa)	σ_y (MPa)	τ_{xy} (MPa)	σ_x (MPa)	σ_y (MPa)	τ_{xy} (MPa)	
K1	−0.08	−0.92	0.42	−0.08	−0.92	0.44	0.99
K2	−0.17	−1.42	0.62	−0.17	−1.42	0.61	1.00
K3	0.00	−7.63	0.00	0.00	−7.63	0.00	1.00
K4	−1.83	0.00	0.00	−1.83	0.00	0.00	1.00
K6	−0.32	−0.32	0.32	−0.32	−0.32	0.34	0.98
K7	−0.39	−2.25	0.93	−0.39	−2.25	0.94	1.00
K8	−0.22	−0.04	0.09	−0.22	−0.04	0.12	0.95
K10	−2.11	−6.44	0.00	−2.15	−6.44	0.00	1.00
K11	−2.04	−4.49	1.23	−2.04	−4.49	1.39	0.99
K12	−2.03	−2.03	1.08	−2.03	−2.03	0.69	1.04

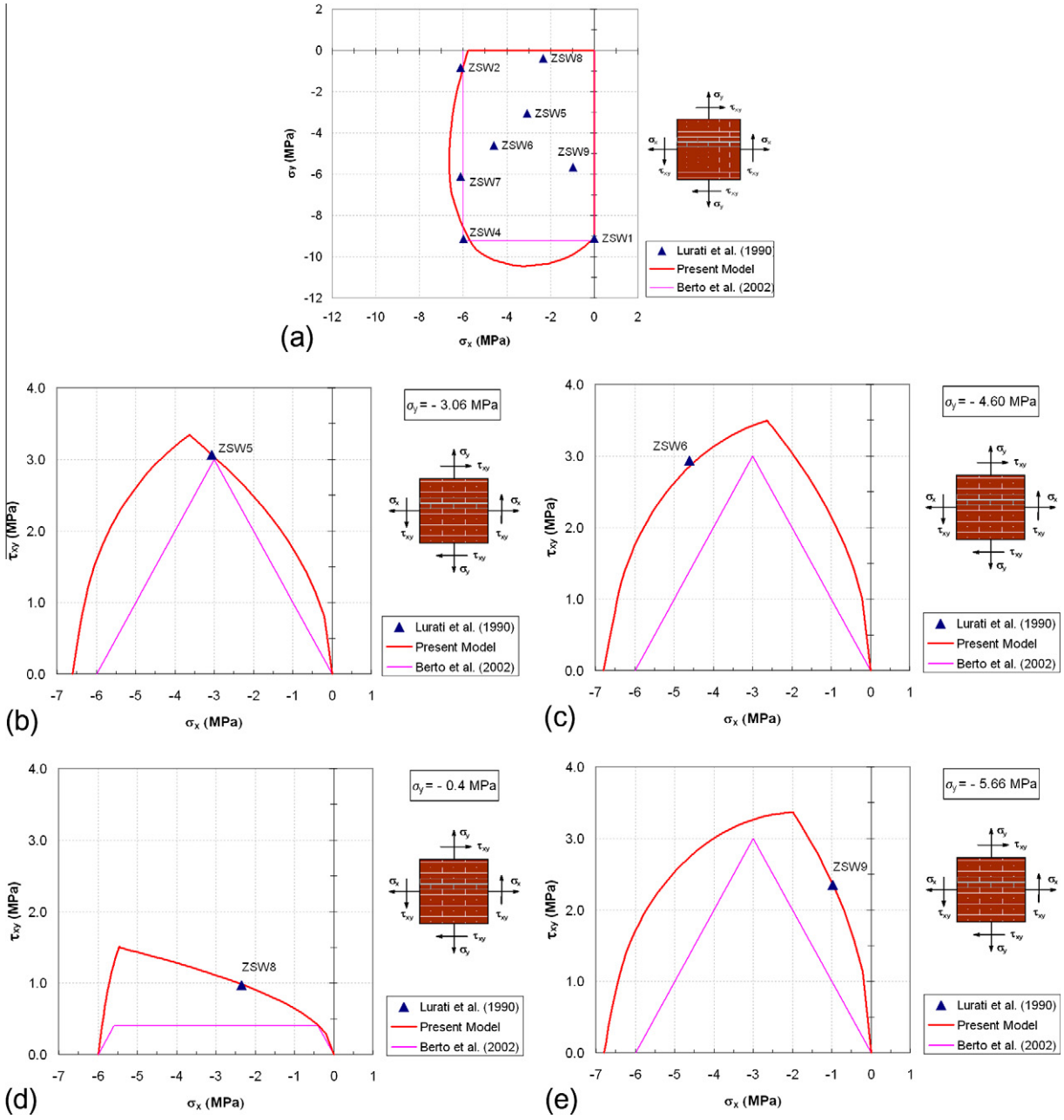

Fig. 8. Comparison between the proposed model, the damage domain formulated by Berto et al. [19] and the experimental results from Lurati et al. [76]: composite failure surface (a) and comparisons with tests ZSW5 (b), ZSW6 (c), ZSW8 (d) and ZSW9 (e).

experiments for these loading conditions (early splitting of the bed joints in tension), see [15]. In fact, the individual "piers" of masonry formed after splitting of the bed joints can withstand a much higher load before collapse is obtained.

Similarities of the proposed composite failure surface with the one by Lourenço et al. are observed. Nevertheless, the Two-Parameters Damage Model that has been presented is more advantageous, because of its intrinsic simplicity. The favourable strain-driven format provides robustness and high algorithmic efficiency, avoiding the problem of possible ill-conditioning of the return-mapping algorithm in stress-driven orthotropic plasticity models [74].

5.2. Simulation of experimental tests conducted by Ganz and Thürlimann

A smaller testing program of biaxially loaded masonry panels was carried out at ETH Zurich. The panels, with dimensions $1200 \times 1200 \times 150\ \text{mm}^3$, were loaded proportionally in the principal stress directions σ_1 and σ_2 along different orientations θ with respect to the material axes as defined previously. The 12 panels of hollow clay brick masonry, denoted by panels K1 to K12 and reported by Ganz and Thürlimann [75], are considered.

The values assumed for real strengths are $f_{11}^{+} = 0.28$ MPa, $f_{22}^{+} = 0.01$ MPa and $f_{12}^{+} = 0.04$ MPa for tension and $f_{11}^{-} = 1.83$ MPa, $f_{22}^{-} = 7.63$ MPa and $f_{12}^{-} = 3.41$ MPa for compression. The parameter K has been considered equal to 0.072. All the aforementioned values have been selected according to data given in [75] and parameters calibrated in [63]. The composite damage criterion features a high degree of anisotropy ($f_x^{+}/f_y^{+} = 28$ and $f_y^{-}/f_x^{-} = 4.17$). These high ratios are due to the high perforation of the clay bricks. For all the tests, the material properties in the 1-axis have been selected for the mapped space. Fig. 7a shows the shape of the adopted composite damage criterion both with the points representing the set of strength experimental data.

The test results, the proposed model results and the ratio between experimental and predicted failure are given in Table 2. Notice that this ratio is a measure of the norm of the stress vector in the $(\sigma_x, \sigma_y, \tau_{xy})$-space which equals $\left(\sigma_x^2 + \sigma_y^2 + \tau_{xy}^2\right)^{1/2}$. Panels K5 and K9 are not included because the boundary conditions affected the failure mode of panel K5 and panel K9 included reinforcement.

The model is able to reproduce the strength behaviour of this type of anisotropic masonry with good accuracy. The error is bounded by a maximum value of 5%, corresponding to test K8. The mean of the ratios results equal to 0.995.

For the sake of completeness, Fig. 7b–h report, for each test, the comparison between the point of coordinates $\sigma_{x,u}$, $\sigma_{y,u}$, $\tau_{xy,u}$, which denote the experimental failure conditions, with the section of the composite damage surface at a constant value of $\sigma_{y,u}$. These figures help to understand better how the proposed methodology models the shear strength behaviour of this type of masonry. It appears that the tension regime represents the majority of the composite damage surface domain.

5.3. Simulation of experimental tests conducted by Lurati et al.

The nine panels of hollow concrete block masonry, denoted by panels ZSW1 to ZSW9 and tested by Lurati et al. [76] as a part of the ETH Zurich program, are considered next. Panel ZSW3 is not considered because the head joints were not filled.

The values assumed for real strengths are $f_{11}^{+} = 0.01$ MPa, $f_{22}^{+} = 0.01$ MPa and $f_{12}^{+} = 0.01$ MPa for tension and $f_{11}^{-} = 5.78$ MPa, $f_{22}^{-} = 9.12$ MPa and $f_{12}^{-} = 3.98$ MPa for compression. This type of masonry is practically a no-tension material. The parameter K has been considered equal to 0.0. All the aforementioned values have been selected according to data given in [76] and parameters calibrated in [63]. The composite damage criterion features a reasonable degree of anisotropy in compression, with $f_y^{-}/f_x^{-} = 1.58$. For all the tests, the material properties in the 1-axis have been selected for the mapped space. Fig. 8a shows the shape of the adopted composite damage criterion both with the points representing the set of strength experimental data. For the sake of comparison, the damage domain formulated by Berto et al. [19] is also reported.

The test results, the proposed model results and the ratio between experimental and predicted failure are given in Table 3. This ratio is again a measure of the norm of the stress vector in the $(\sigma_x, \sigma_y, \tau_{xy})$-space which equals $\left(\sigma_x^2 + \sigma_y^2 + \tau_{xy}^2\right)^{1/2}$.

The model is also able to reproduce the strength behaviour of this type of anisotropic masonry with good accuracy. The error is bounded by a maximum value of 7%, corresponding to test ZSW7. The mean of the ratios results equal to 0.993.

For the sake of completeness, Fig. 8b–e report, for each test, the comparison between the point of coordinates $\sigma_{x,u}$, $\sigma_{y,u}$, $\tau_{xy,u}$, which denote the experimental failure conditions, with the section of the composite damage surface at a constant value of $\sigma_{y,u}$. As can be seen, the proposed model is able to capture the correct shear strength of this orthotropic masonry. As shown by Fig. 8c–e, the damage domain formulated by Berto et al. leads to conservative values and cannot model the increase of strength in biaxial compression, since the failure surface is defined as a simple straight-sided rectangle in the $\sigma_x - \sigma_y$ plane.

6. Conclusions

In this paper, a plane-stress macro-model for orthotropic masonry has been presented.

The proposed model is capable of modelling:

- the elastic orthotropy of the intact material;
- different strength along the two natural directions of masonry, parallel and orthogonal to the mortar joints;

Table 3
Comparison between the proposed model and the experimental results obtained by Lurati et al. [76].

Panel	Experimental results			Present model			Ratio
	σ_x (MPa)	σ_y (MPa)	τ_{xy} (MPa)	σ_x (MPa)	σ_y (MPa)	τ_{xy} (MPa)	
ZSW1	0.00	−9.12	0.00	0.00	−9.12	0.00	1.00
ZSW2	−6.12	−0.83	0.00	−6.01	−0.83	0.00	1.02
ZSW4	−5.98	−9.13	0.00	−5.76	−9.12	0.00	1.01
ZSW5	−3.06	−3.06	3.06	−3.06	−3.06	3.07	1.00
ZSW6	−4.60	−4.60	2.93	−4.60	−4.60	3.06	0.99
ZSW7	−6.12	−6.12	0.00	−6.60	−6.60	0.00	0.93
ZSW8	−2.34	−0.40	0.97	−2.34	−0.40	0.98	1.00
ZSW9	−0.97	−5.66	2.35	−0.97	−5.66	2.36	1.00

- different softening behaviour along these two directions;
- the dependence of the response on the inclination of the natural axes of the material;
- the unloading (and reloading) depending on the damaged stiffness;
- the stiffness recovery at crack closure under alternate loading.

The damage model is based on the concept of *mapped tensor* from the orthotropic real space. A one-to-one mapping relationship is established between the orthotropic behaviour and an auxiliary model. The problem is solved in the mapped space and the results are transported to the real field.

In order to account for different behaviour in tension and compression, the relationship between the two spaces is defined by means of two *transformation tensors*, which are related to tensile stress states and compressive stress states, respectively. Such an enhancement of the original Betten's model permits to reproduce different ultimate behaviours in tension and compression by considering two distinct isotropic criteria in the mapped space. Each of them describes different failure mechanisms. The first criterion is associated with a localized fracture process, namely cracking of the material, and the second criterion is associated with a more distributed fracture process, i.e. the crushing of the material. In this study, a Rankine criterion for tension and a Faria criterion in compression have been selected for the mapped space.

It is possible to adjust the two assumed isotropic criteria to the particular behaviour of the orthotropic material. In fact, the two distinct transformations allow us to scale in distinct manners the two isotropic failure surfaces assumed in the mapped space. The result is an implicit composite failure surface defined in the real space.

The constitutive model assumed in the mapped space is the Tension–Compression Damage Model [47–54]. An essential feature of the proposed model is that a split into tensile and compressive contributions is introduced. The model includes different hardening/softening behaviour for tension and compression. The damage variables are related by an equivalent length to the released energy per unit cracked area.

The orthotropic nature of the Tension–Compression Damage Model adopted in the mapped space has been demonstrated, although it has usually been termed as "isotropic" in the available literature. This feature, both with the assumption of two distinct damage criteria for tension and compression, does not permit to term the mapped space as "isotropic". Therefore, the present methodology turns the original concept of "mapping the real space into an *isotropic* auxiliary one" into the innovative and more general one of "mapping the real space into a *favourable* (or *convenient*) auxiliary one".

The model has been fully formulated for the two-dimensional case but it can be easily extended to the three-dimensional one by providing additional material parameters [45].

The strength parameters involved appear to be enough to reproduce the biaxial failure of all masonry types, ranging from isotropic to extreme anisotropic behaviours. This validation has been carried out by means of comparisons with experimental results on different types of orthotropic masonry. Compared to other existing macro-models available in literature, the proposed strategy affords an improved prediction of the experimental evidence with regard to the obtained failure locus. A full appraisal of the directional dependence of the softening behaviour still needs further validation.

Acknowledgments

The studies presented here have been developed within the research projects BIA2006-04127 and SEDUREC (CSD2006-00060) funded by DGE of the Spanish Ministry of Science and Technology, whose assistance is gratefully acknowledged. The authors thank Prof. Sergio Oller for his helpful suggestions.

References

[1] A.W. Hendry, Structural Masonry, Macmillan Education, London, 1990.
[2] R.G. Drysdale, A.A. Hamid, L.R. Baker, Masonry Structures: Behavior and Design, Prentice-Hall, Englewood Cliffs, New Jersey, 1994.
[3] P. Roca, M. Cervera, G. Gariup, L. Pelà, Structural analysis of masonry historical constructions. Classical and advanced approaches, Arch. Comput. Methods Engrg. 17 (2010) 299–325.
[4] A.W. Page, Finite element model for masonry, J. Struct. Div. 104 (1978) 1267–1285.
[5] W. Samarasinghe, A.W. Page, A.W. Hendry, Behaviour of masonry shear walls, Struct. Engrg. 59 (1981) 42–48.
[6] G.N. Pande, J.X. Liang, J. Middleton, Equivalent elastic moduli for brick masonry, Comput. Geotech. 8 (1989) 243–265.
[7] S. Pietruszczak, X. Niu, A mathematical description of macroscopic behaviour of brick masonry, Int. J. Solids Struct. 29 (1992) 531–546.
[8] A. Anthoine, Derivation of the in-plane elastic characteristics of masonry through homogenization theory, Int. J. Solids Struct. 32 (1995) 137–163.
[9] A. Zucchini, P.B. Lourenço, A micro-mechanical model for the homogenisation of masonry, Int. J. Solids Struct. 39 (2002) 3233–3255.
[10] A. Cecchi, K. Sab, A multi-parameter homogenization study for modeling elastic masonry, Eur. J. Mech. A/Solids 21 (2002) 249–268.
[11] F.Y. Yokel, S.G. Fattal, Failure hypothesis for masonry shear walls, J. Struct. Div. 102 (1976) 515–532.
[12] W. Mann, H. Müller, Failure of shear-stressed masonry – an enlarged theory, tests and application to shear walls, Proc. Brit. Ceram. Soc. 30 (1982) 223–235.
[13] A.W. Page, The biaxial compressive strength of brick masonry, Proc. Inst. Civil Engrg. 71 (1981) 893–906.
[14] A.W. Page, The strength of brick masonry under biaxial tension–compression, Int. J. Masonry Constr. 3 (1983) 26–31.
[15] M. Dhanasekar, A.W. Page, P.W. Kleeman, The failure of brick masonry under biaxial stresses, Proc. Inst. Civil Engrg. 79 (1985) 295–313.
[16] H.R. Ganz, B. Thürlimann, Strength of brick walls under normal force and shear, in: Proc. 8th International Symposium on Load Bearing Brickwork, London, 1983.
[17] S.W. Tsai, E.M. Wu, A general theory of strength for anisotropic materials, J. Compos. Mater. 5 (1971) 58–80.
[18] C.A. Syrmakezis, P.G. Asteris, Masonry failure criterion under biaxial stress state, J. Mater. Civil. Engrg. 13 (2001) 58–64.
[19] L. Berto, A. Saetta, R. Scotta, R. Vitaliani, An orthotropic damage model for masonry structures, Int. J. Numer. Methods Engrg. 55 (2002) 127–157.
[20] O. Hoffman, The brittle strength of orthotropic materials, J. Compos. Mater. 1 (1967) 200–206.
[21] P.B. Lourenço, Computational Strategy for Masonry Structures, Delft University Press, 1996.
[22] P.H. Feenstra, R. De Borst, A composite plasticity model for concrete, Int. J. Solids Struct. 33 (1996) 707–730.
[23] D.C. Drucker, W. Prager, Solid mechanics and plastic analysis for limit design, Quart. Appl. Math. 10 (1952) 157–165.
[24] P.B. Lourenço, R. De Borst, J.G. Rots, Plane stress softening plasticity model for orthotropic materials, Int. J. Numer. Methods Engrg. 40 (1997) 4033–4057.
[25] G. Alpa, I. Monetto, Microstructural model for dry block masonry walls with inplane loading, J. Mech. Phys. Solids 42 (1994) 1159–1175.
[26] L. Gambarotta, S. Lagomarsino, A microcrack damage model for brittle materials, Int. J. Solids Struct. 30 (1993) 177–198.
[27] L. Gambarotta, S. Lagomarsino, Damage models for the seismic response of brick masonry shear walls. Part I: The mortar joint model and its applications, Earthq. Engrg. Struct. D 26 (1997) 423–439.
[28] L. Gambarotta, S. Lagomarsino, Damage models for the seismic response of brick masonry shear walls. Part II: The continuum model and its applications, Earthq. Engrg. Struct. D 26 (1997) 441–462.
[29] E. Papa, A unilateral damage model for masonry based on a homogenisation procedure, Mech. Cohes.-Frict. Mater. 1 (1996) 349–366.
[30] T.J. Massart, R.H.J. Peerlings, M.G.D. Geers, Mesoscopic modeling of failure and damage-induced anisotropy in brick masonry, Eur. J. Mech. A/Solids 23 (2004) 719–735.
[31] G. Milani, P.B. Lourenço, A. Tralli, Homogenised limit analysis of masonry walls. Part I: Failure Surfaces, Comput. Struct. 84 (2006) 166–180.
[32] G. Milani, P.B. Lourenço, A. Tralli, Homogenised limit analysis of masonry walls. Part II: Structural Examples, Comput. Struct. 84 (2006) 181–195.
[33] P.B. Lourenço, G. Milani, A. Tralli, A. Zucchini, Analysis of masonry structures: review and recent trends of homogenisation techniques, Can. J. Civil Engrg. 34 (2007) 1443–1457.
[34] E. Sacco, A nonlinear homogenization procedure for periodic masonry, Eur. J. Mech. A/Solids 28 (2009) 209–222.
[35] G. Uva, G. Salerno, Towards a multiscale analysis of periodic masonry brickwork: a FEM algorithm with damage and friction, Int. J. Solids Struct. 43 (2006) 3739–3769.

[36] S. Brasile, R. Casciaro, G. Formica, Multilevel approach for brick masonry walls. Part I: A numerical strategy for the nonlinear analysis, Comput. Methods Appl. Mech. Engrg. 196 (2007) 4934–4951.
[37] T.J. Massart, R.H.J. Peerlings, M.G.D. Geers, Structural damage analysis of masonry walls using computational homogenisation, Int. J. Damage Mech. 16 (2007) 199–226.
[38] T.J. Massart, R.H.J. Peerlings, M.G.D. Geers, An enhanced multi-scale approach for masonry wall computations with localization of damage, Int. J. Numer. Methods Engrg. 69 (2007) 1022–1059.
[39] B.C.N. Mercatoris, T.J. Massart, Assessment of periodic homogenization-based multiscale computational schemes for quasi-brittle structural failure, Int. J. Multiscale Comput. Engrg. 7 (2009) 153–170.
[40] L.A. Mihai, M. Ainsworth, An adaptive multi-scale computational modelling of Clare College Bridge, Comput. Methods Appl. Mech. Engrg. 198 (2009) 1839–1847.
[41] J. Betten, Creep Theory of Anisotropic Solids, J. Rheol. 25 (1981) 565–581.
[42] J. Betten, Applications of tensor functions to the formulation of yield criteria for anisotropic materials, Int. J. Plasticity 4 (1988) 29–46.
[43] S. Oller, S. Botello, J. Miquel, E. Oñate, An anisotropic elastoplastic model based on an isotropic formulation, Engrg. Comput. 12 (1995) 245–262.
[44] S. Oller, E. Oñate, J. Miquel, Mixing anisotropic formulation for analysis of composites, Commun. Numer. Methods Engrg. 12 (1996) 471–482.
[45] S. Oller, E. Car, J. Lubliner, Definition of a general implicit orthotropic yield criterion, Comput. Methods Appl. Mech. Engrg. 192 (2003) 895–912.
[46] L. Pelà, Continuum Damage Model for Nonlinear Analysis of Masonry Structures, Ph.D. Thesis, Technical University of Catalonia, University of Ferrara, 2009.
[47] R. Faria, J. Oliver, A Rate Dependent Plastic-Damage Constitutive Model for Large Scale Computations in Concrete Structures, CIMNE Monograph 17, Technical University of Catalonia, 1993.
[48] R. Faria, J. Oliver, M. Cervera, A strain-based plastic viscous-damage model for massive concrete structures, Int. J. Solids Struct. 35 (1998) 1533–1558.
[49] R. Faria, J. Oliver, M. Cervera, On Isotropic Scalar Damage Models for the Numerical Analysis of Concrete Structures, CIMNE Monograph PI198, Technical University of Catalonia, 2000.
[50] R. Faria, J. Oliver, M. Cervera, Modeling material failure in concrete structures under cyclic actions, J. Struct. Engrg. 130 (2004) 1997–2005.
[51] M. Cervera, J. Oliver, R. Faria, Seismic evaluation of concrete dams via continuum damage models, Earthq. Engrg. Struct. D 24 (1995) 1225–1245.
[52] M. Cervera, J. Oliver, O. Manzoli, A rate-dependent isotropic damage model for the seismic analysis of concrete dams, Earthq. Engrg. Struct. D 25 (1996) 987–1010.
[53] M. Cervera, J. Oliver, T. Prato, Thermo-chemo-mechanical model for concrete. II: Damage and creep, J. Engrg. Mech. 125 (1999) 1028–1039.
[54] M. Cervera, Viscoelasticity and Rate-Dependent Continuum Damage Models, CIMNE, Monograph No. 79, Technical University of Catalonia, 2003.
[55] P. Pegon, A. Anthoine, Numerical strategies for solving continuum damage problems with softening: application to the homogenization of masonry, Comput. Struct. 64 (1997) 623–642.
[56] J. Lemaitre, J.L. Chaboche, Aspects phénoménologiques de la rupture par endommagement, J. Méc. Appl. 2 (1978) 317–365.
[57] J.Y. Wu, J. Li, On the mathematical and thermodynamical descriptions of strain equivalence based anisotropic damage model, Mech. Mater. 40 (2008) 377–400.
[58] J.C. Simó, J.W. Ju, Strain- and stress-based continuum damage models – I. Formulation, Int. J. Solids Struct. 23 (1987) 821–840.
[59] M. Cervera, L. Pelà, R. Clemente, P. Roca, A crack-tracking technique for localized damage in quasi-brittle materials, Engrg. Fract. Mech. 77 (2010) 2431–2450.
[60] Z.P. Bazant, B.H. Oh, Crack band theory for fracture of concrete, Mater. Struct. 16 (1983) 155–177.
[61] E. Car, S. Oller, E. Oñate, Algorithmic tangent matrices in the elastoplastic problem (in Spanish), in: Proceedings of the XVIII Spanish American Congress on Computational Methods in Engineering (CILAMCE), vol. IV, Brasilia, 1997, pp. 2039–2051.
[62] A. Pérez-Foguet, A. Rodríguez-Ferran, A. Huerta, Numerical differentiation for local and global tangent operators in computational plasticity, Comput. Methods Appl. Mech. Engrg. 189 (2000) 277–296.
[63] P.B. Lourenço, J.G. Rots, J. Blaauwendraad, Continuum model for masonry: parameter estimation and validation, J. Struct. Engrg. 124 (1998) 642–652.
[64] M. Dhanasekar, W. Haider, Explicit finite element analysis of lightly reinforced masonry shear walls, Comput. Struct. 86 (2008) 15–26.
[65] P. Trovalusci, R. Masiani, Non-linear micropolar and classical continua for anisotropic discontinuous materials, Int. J. Solids Struct. 40 (2003) 1281–1297.
[66] G. Pijaudier-Cabot, Z.P. Bazant, Nonlocal damage theory, J. Engrg. Mech. 113 (1987) 1512–1533.
[67] R.H.J. Peerlings, R. De Borst, W.A.M. Brekelmans, J.H.P. De Vree, Gradient enhanced damage for quasi-brittle materials, Int. J. Numer. Methods Engrg. 39 (1996) 3391–3403.
[68] M. Cervera, M. Chiumenti, Q. Valverde, C. Agelet de Saracibar, Mixed linear/linear simplicial elements for incompressible elasticity and plasticity, Comput. Methods Appl. Mech. Engrg. 192 (2003) 5249–5263.
[69] M. Cervera, M. Chiumenti, C. Agelet de Saracibar, Softening, localization and stabilization: capture of discontinuous solutions in J2 plasticity, Int. J. Numer. Anal. Methods Geomech. 28 (2004) 373–393.
[70] M. Cervera, M. Chiumenti, C. Agelet de Saracibar, Shear band localization via local J2 continuum damage mechanics, Comput. Methods Appl. Mech. Engrg. 193 (2004) 849–880.
[71] M. Cervera, M. Chiumenti, Size effect and localization in J2 plasticity, Int. J. Solids Struct. 46 (2009) 3301–3312.
[72] M. Cervera, M. Chiumenti, R. Codina, Mixed stabilized finite element methods in nonlinear solid mechanics. Part I: Formulation, Comput. Methods Appl. Mech. Engrg. 199 (2010) 2559–2570.
[73] M. Cervera, M. Chiumenti, R. Codina, Mixed stabilized finite element methods in nonlinear solid mechanics. Part II: Strain localization, Comput. Methods Appl. Mech. Engrg. 199 (2010) 2571–2589.
[74] P.B. Lourenço, J.G. Rots, P.H. Feenstra, A "tensile" Rankine-type orthotropic model for masonry, in: G.N. Pande, J. Middleton (Eds.), Computer Methods in Structural Masonry, vol. 3, Books & Journals International, Swansea, 1995.
[75] H.R. Ganz, B. Thürlimann, Tests on the biaxial strength of masonry (in German), Report No. 7502-3, Institute of Structural Engineering, ETH Zurich, 1982.
[76] F. Lurati, H. Graf, B. Thürlimann, Experimental determination of the strength parameters of concrete masonry (in German), Report No. 8401-2, Institute of Structural Engineering, ETH Zurich, 1990.